Highly Sensitive Polarimetric Sensor Based on Fano Resonance for DNA Hybridization Detection

Xiang Zhao[1] · Tianye Huang[1] · Shuwen Zeng[2] · Chaolong Song[1] · Zhuo Cheng[1] · Xu Wu[1] · Pan Huang[1] · Jianxing Pan[1] · Yiheng Wu[1] · Perry Ping Shum[3]

Abstract

Surface plasmon resonance (SPR) sensor based on reflectivity measurement has been widely studied for its convenient detection, high sensitivity, and real-time functions. However, the resonance curves of SPR reflectivity spectrum are broad that lead to a low detection limit (DL) and low detection resolution. In this work, Fano resonance (FR), which has an asymmetrical sharp and narrow resonance peak, is demonstrated here to improve the DL and resolution of the plasmonic sensor. More importantly, a three-point method is employed here to analyzed and extract the polarization information of the reflected light by replacing the conventional intensity interrogation method. The sharp signal change of the Fano resonance realized by the designed configuration together with the three-point method led to a significantly enhancement on the DL and the resolution of the FR-based sensor up to one order of magnitude comparing to conventional scheme commonly used with the commercial products. Thus, the proposed sensor is of great potential for biochemical sensing such as DNA detection in terms of measuring the refractive index change at the sensing interface.

Keywords Fano resonance · Three-point method · Detection limit · Biochemical sensing

Introduction

Surface plasmon resonance (SPR) is an optical phenomenon that occurs between two materials with negative and positive real parts of dielectric constants [1], respectively. When the parallel wave vector of incident light is matched with the propagation constant of the surface plasmon, free electrons on the metal surface can resonant with the incident photons and absorb light energy, thus causing a sharp attenuation of reflected light [2]. Due to the advantages of convenient detection, high sensitivity, and real-time functions, SPR sensors are widely applied to chemical and biomolecular detection [3–5]. However, the performance of the conventional SPR sensors is restricted by its broad resonance curve which corresponds to a low resolution or detection limit (DL) of the sensors. Therefore, to obtain a sharper resonance curve has become a research hotspot. For this purpose, different approaches including long-range surface plasmon resonance (LRSPR) [6], waveguide-coupled SPRs [7], and Au-Ag bimetallic hybrid structure [8] have been presented to achieve this goal in the past decades.

Recently, Fano resonance (FR), which is induced by the coupling between the dark mode and the bright mode in the resonance system, is regarded an effective way to further improve the sensing performance [9–14]. In such structures, the surface plasmon polariton (SPP) mode generated at metal-dielectric interface and the planar waveguide mode (PWG) formed in dielectric multilayers interact with each other through the superposition of evanescent field. The FR is characterized by an asymmetrical line shape resulting in sharp intensity variation between resonance peak and dip. The Kretschmann-Raether (KR) configuration with attenuated total reflection (ATR) is widely employed for building SPR sensors [1]. By monitoring the variation of the reflectance curve or the position of the resonance, the refractive index changes in the sensing medium can be measured to detect chemical and biomolecular changes. Currently, the investigations for most FR-based sensors mainly focus on intensity interrogation due to the availability of miniature and low-cost

✉ Tianye Huang
tianye_huang@163.com

✉ Zhuo Cheng
Chengzhuo@cug.edu.cn

[1] School of Mechanical Engineering and Electronic Information, China University of Geosciences (Wuhan), Wuhan 430074, China

[2] XLIM Research Institute, UMR 7252 CNRS/University of Limoges, 123, Avenue Albert Thomas, 87060 Limoges Cedex, France

[3] Center of Fiber Technology, Electrical and Electronics Engineering, Nanyang Technological University, Singapore, Singapore

spectrometers. However, it is suggested phase interrogation is able to offer even lower DL since the phase response can be more than one order of magnitude drastic than the intensity [14–17]. It should be noted that, similar with conventional SPR, it is proved that there should also be a drastic phase change near the FR and how this kind of phase change contributing to the sensing performance is worthy revealing.

In general, it is necessary to measure the light intensities first in order to retrieve the phase information. Therefore, they are very sensitive to intensity noise of the incident waves. Currently, phase measurement setups such as interferometry [16–22], optical heterodyning [23–27], and polarimetry [28–32] can be used to extract the phase information. Among them, polarimetric setups have the advantage that it can be applied to spectroscopic measurements based on the polarization characteristics variation of light which is much simple. Naraoka et al. proposed the rotating analyzer method, which adds only a rotatable analyzer to the conventional SPR apparatus. A linearly polarized light is incident on the sample, and the reflectance is measured as a function of the angle of analyzer rotation to provide a phase difference between the p-polarized and the s-polarized reflected light [28]. Markowicz et al. introduced a phase-sensitive SPR polarimetry scheme, which uses a photo-elastic modulator to mix the polarized beam reflected by the SPR sensor. The proposed configuration provided a much lower detection limit to refractive index and also a wide dynamic range of measurements [33]. I. Watad presented a spectropolarimetric SPR sensor with only a polarizer and a polarization analyzer. By measuring the reflected intensities at different polarization angles, the phase variation can be extracted through post signal-processing algorithms [32].

In this paper, a prism-metal-dielectric-dielectric-analyte multilayer configuration is proposed for generating FR and constructing highly sensitive refractive index sensor. It is demonstrated that similar to that of conventional SPR, there also exists a sharp phase jump near the FR which is suitable for phase interrogation. Based on this platform, a three-point polarimetric method is used to analyze the FR-based sensing performance for the first time. Profiting from the advantages of FR, a DL of 6.2×10^{-9} RIU is predicted even under the consideration of system noise. Such configuration is investigated for DNA renaturation as well; the results show that the DL can be enhanced up to one order.

Design Consideration and Theoretical Model

The polarimetric setup of FR is presented in Fig. 1. A collimating objective converts light beam from divergent to parallel through a polarizer which is 45° with respect to the p-polarization direction. It is then incident into the multilayer structure. The reflected beam passes through an analyzer which orients at a specific angle corresponding to the p-polarization direction. Since p- and s-polarization component

experience different amplitudes and phase shifts, they will interfere with each other in the analyzer. The interference pattern is collected by the spectrometer for post-processing.

We define the reflectivity R as follows:

$$R = \frac{I_P}{I_S} = \frac{R_P}{R_S} = \left|\frac{r_P}{r_S}\right|^2 \tag{1}$$

where r_p and r_s are the reflection coefficients of p- and s-polarization component, and φ_p and φ_s are the phase of p- and s-polarization components. Supposing the reflections between different layers in the sensor construction are ignored, the signal intensity I tested at output terminal is given as follows [32]:

$$I = \frac{I_0}{2}\left[1 + \tan^2\psi + (\tan^2\psi - 1)\cos 2A + 2\tan\psi\cos\Delta\sin 2A\right] \tag{2}$$

where I_0 is the intensity of white light source, A is the rotation angle of the analyzer, $\Delta = \varphi_p - \varphi_s$ is phase difference between p- and s-polarization components, and ψ is the azimuth angle of a polarization ellipse of the reflected light; cosine of Δ and tangent of ψ can be figured out theoretically from normalized reflection coefficients of p- and s-polarization components by the following:

$$\tan\psi = \left|\frac{r_P}{r_S}\right| \tag{3}$$

$$\cos\Delta = \cos\left(-i\log\left(\frac{r_P/|r_P|}{r_S/|r_S|}\right) + 2n\pi\right), n = 0, \pm 1, \pm 2, ... \tag{4}$$

In order to obtain the values respectively for I, ψ, and Δ in Eq. (2), three measurements are used to obtain relevant information. In three-point polarimetric method, the analyzer is rotated in three different directions for three measurements. The rotation angle of the analyzer A is oriented at $-45°$, $0°$, and $45°$, representing vertical, 45°, and parallel direction with respect to the angle of the polarizer. Output signals $I_\perp$, I_{45}, and $I_\parallel$ corresponding to three rotation angles can be expressed as follows:

$$I_\perp = \frac{I_0}{4}\cdot(1 + \tan^2\psi - 2\tan\psi\cos\Delta) \tag{5}$$

$$I_{45} = \frac{I_0}{2}\tan^2\psi \tag{6}$$

$$I_\parallel = \frac{I_0}{4}\cdot(1 + \tan^2\psi + 2\tan\psi\cos\Delta) \tag{7}$$

According to these three equations, tangent of ψ and cosine of Δ can be calculated by the following:

$$\tan\psi = \sqrt{\frac{I_{45}}{I_\perp + I_\parallel - I_{45}}} \tag{8}$$

$$\cos\Delta = \frac{I_\parallel - I_\perp}{2\tan\psi(I_\parallel + I_\perp - I_{45})} \tag{9}$$

Through Eq. (8) and Eq. (9), the phase difference between p- and s-polarization components and the azimuth angle of the polarization ellipse of reflected light can be obtained from the intensity measurement. Furthermore, since the polarization parameters are acquired from the ratio of intensity, the influence of intensity fluctuation of light source can be removed [32]. Comparing to conventional spectral measurement which requires a reference spectrum, the extraction of the polarization functions from the intensity ratio eliminates the need to obtain the reference spectrum in each measurement and makes the measurement process more convenient.

The schematic diagram of the proposed FR transducer in Fig. 1 is a typical Kretschmann configuration. Here, the configuration consists of five layers. The metal used in this configuration is Au with refractive index $n_{Au} = 0.2184 + 3.5113i$, and the incident wavelength is assumed to be 632.8 nm [34]. When a semi-infinite dielectric layer which employs SF10 prism with $n_p = 1.723$ approaches the Au layer, the structure can excite SPP modes propagating along the SF10-Au interface and provide a broad resonance in the reflectance spectrum. Meanwhile, there are three dielectric layers supporting PWG mode. Since the TiO$_2$ possesses higher refractive index ($n_2 = 2.3894$) than its neighborhood cytop (1.340) and sensing medium (~ 1.332) [9], PWG modes can be formed within such three-layer structure. Particularly, the evanescent fields of the SPP and PWG modes overlap with each other in the cytop spacer layer resulting in mode hybridization. The thickness of Au layer is fixed at 50 nm which leads to the deepest and narrowest SPR. The proposed Fano resonance sensor can be fabricated through bottom-up process. Firstly, the Au film is evaporation on the glass substrate [35]. Then, the thick cytop layer can be formed by using spin-coating [36]. Thirdly, the TiO$_2$ layer is deposited on the cytop layer [37]. Finally, the prism can be attached to the substrate through index match oil. To analyze the fabrication tolerance, the resonance features of both polarization functions and reflectivity obtained for the different thickness of cytop (a–c) and TiO$_2$ (d–f) are represented in Fig. 2. The thickness intervals of cytop and TiO$_2$ are 5 nm and 1 nm, respectively. It can be found that there is no signicant line shape changes due to the thickness variation. The resonance angle shifts to large angle with thickness increment. However, such resonance angle variation does not have significant impacts on the sensing performance in the proposed sensing scheme.

In the conventional SPR system, the noise of measurement signals origins from many sources, such as temperature change, mechanical instability, source strength fluctuation, and detector noise source [15, 38–41], while in the polarimetric system, the influence of intensity fluctuation is known to be eliminated by intensity ratios in different directions [32]. Therefore, only two noise sources are considered, namely the fluctuation of detection intensity ΔI, and the accuracy of the rotation phase of the analyzer ΔA. Considering the influence of two kinds of noise, the noise of tangent of the azimuth angle $<\Delta\tan\psi>_{min}$ can be expressed as follows [42]:

$$\langle\Delta\tan\psi\rangle_{min} = \left(\left(\frac{\partial\tan\psi}{\partial A}\Big|_{A=-45°}\langle\Delta A|_{A=-45°}\rangle_{min}\right)^2 + \left(\frac{\partial\tan\psi}{\partial A}\Big|_{A=0°}\langle\Delta A|_{A=0°}\rangle_{min}\right)^2 + \left(\frac{\partial\tan\psi}{\partial A}\Big|_{A=45°}\langle\Delta A|_{A=45°}\rangle_{min}\right)^2 \right.$$
$$\left. + \left(\frac{\partial\tan\psi}{\partial I_\perp}\langle\Delta I_\perp\rangle_{min}\right)^2 + \left(\frac{\partial\tan\psi}{\partial I_{45}}\langle\Delta I_{45}\rangle_{min}\right)^2 + + \left(\frac{\partial\tan\psi}{\partial I_\parallel}\langle\Delta I_\parallel\rangle_{min}\right)^2 \right)^{1/2} \quad (10)$$
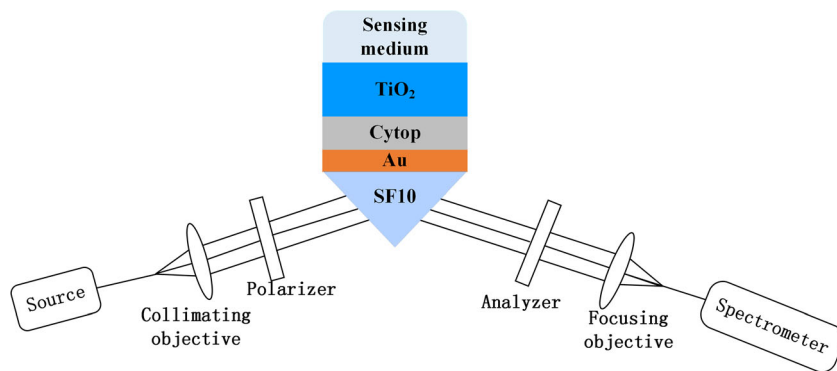
where

$$\begin{array}{ll}
\frac{\partial\tan\psi}{\partial A}\Big|_{A=-45°} = \frac{\tan\psi(1-\tan^2\psi)}{2} & \frac{\partial\tan\psi}{\partial I_\perp} = \frac{-\tan\psi}{I_0} \\
\frac{\partial\tan\psi}{\partial A}\Big|_{A=0°} = \cos\Delta(1+\tan^2\psi) & \frac{\partial\tan\psi}{\partial I_{45}} = \frac{1+\tan^2\psi}{I_0\tan\psi} \\
\frac{\partial\tan\psi}{\partial A}\Big|_{A=45°} = \frac{\tan\psi(\tan^2\psi-1)}{2} & \frac{\partial\tan\psi}{\partial I_\parallel} = \frac{-\tan\psi}{I_0}
\end{array} \quad (11)$$

and the noise of cosine of the phase difference $<\Delta\cos\Delta>_{min}$ can be expressed as follows:

$$\langle\Delta\cos\Delta\rangle_{min} = \left(\left(\frac{\partial\cos\Delta}{\partial A}\Big|_{A=-45°}\langle\Delta A|_{A=-45°}\rangle_{min}\right)^2 + \left(\frac{\partial\cos\Delta}{\partial A}\Big|_{A=0°}\langle\Delta A|_{A=0°}\rangle_{min}\right)^2 + \left(\frac{\partial\cos\Delta}{\partial A}\Big|_{A=45°}\langle\Delta A|_{A=45°}\rangle_{min}\right)^2 \right.$$
$$\left. + \left(\frac{\partial\cos\Delta}{\partial I_\perp}\langle\Delta I_\perp\rangle_{min}\right)^2 + \left(\frac{\partial\cos\Delta}{\partial I_{45}}\langle\Delta I_{45}\rangle_{min}\right)^2 + \left(\frac{\partial\cos\Delta}{\partial I_\parallel}\langle\Delta I_\parallel\rangle_{min}\right)^2 \right)^{1/2} \quad (12)$$

Fig. 1 The polarimetric spectral setup for multilayer structure that generates the FR

where

$$\left.\frac{\partial \cos\Delta}{\partial A}\right|_{A=-45°} = \frac{1-\tan^2\psi}{2\cdot\left(\cos\Delta + \frac{1}{\tan\psi}\right)^{-1}} \quad \frac{\partial \cos\Delta}{\partial I_\perp} = \frac{1+3\tan\psi\cos\Delta}{I_0\tan\psi}$$

$$\left.\frac{\partial \cos\Delta}{\partial A}\right|_{A=0°} = \frac{-\tan\psi\cos\Delta}{\left(1+\tan^2\psi + 2\cos^2\Delta\right)^{-1}} \quad \frac{\partial \cos\Delta}{\partial I_{45}} = \frac{\cos\Delta(\tan^2\psi-1)}{I_0\tan^2\psi} \quad (13)$$

$$\left.\frac{\partial \cos\Delta}{\partial A}\right|_{A=45°} = \frac{\tan^2\psi-1}{2\cdot\left(3\cos\Delta - \frac{1}{\tan\psi}\right)^{-1}} \quad \frac{\partial \cos\Delta}{\partial I_\|} = \frac{1-\tan\psi\cos\Delta}{I_0\tan\psi}$$

In the proposed system, the noise values of the rotation precision of the analyzer in three rotation directions $<\Delta A|_{A=-45°}>_{\min}$, $<\Delta A|_{A=0°}>_{\min}$, and $<\Delta A|_{A=45°}>_{\min}$ are assumed as 0.0005, and the mean noise values of the detected intensity for three orientations between polarizer and analyzer $<\Delta I_\perp>_{\min}$, $<\Delta I_{45}>_{\min}$, and $<\Delta I_\|>_{\min}$ are assumed as 10 counts. Reflectivity is considered for comparison and the noise of reflectivity $<\Delta R>_{\min}$ is represented by the following:

$$\langle\Delta R\rangle_{\min} = \left(\left(\frac{\langle\Delta I_P\rangle}{I_S}\right)^2 + \left(\frac{I_P}{I_S^2}\cdot\langle\Delta I_S\rangle\right)^2\right)^{1/2} \quad (14)$$

where I_p and I_s are the detected intensities with the polarizer points in the p- and s-polarization directions, and the mean noise values of p- and s-detected intensities are assumed as 10 counts, respectively. The equations for the polarimetric measurement and reflectivity are taken from [42].

The quality of the sensor is usually judged by its performance indicators; in this paper, DL is used as parameters to evaluate sensor performance, which are analyzed and calculated by the modified center-of-mass algorithm [32, 42–44]. The FOM can be defined as follows:

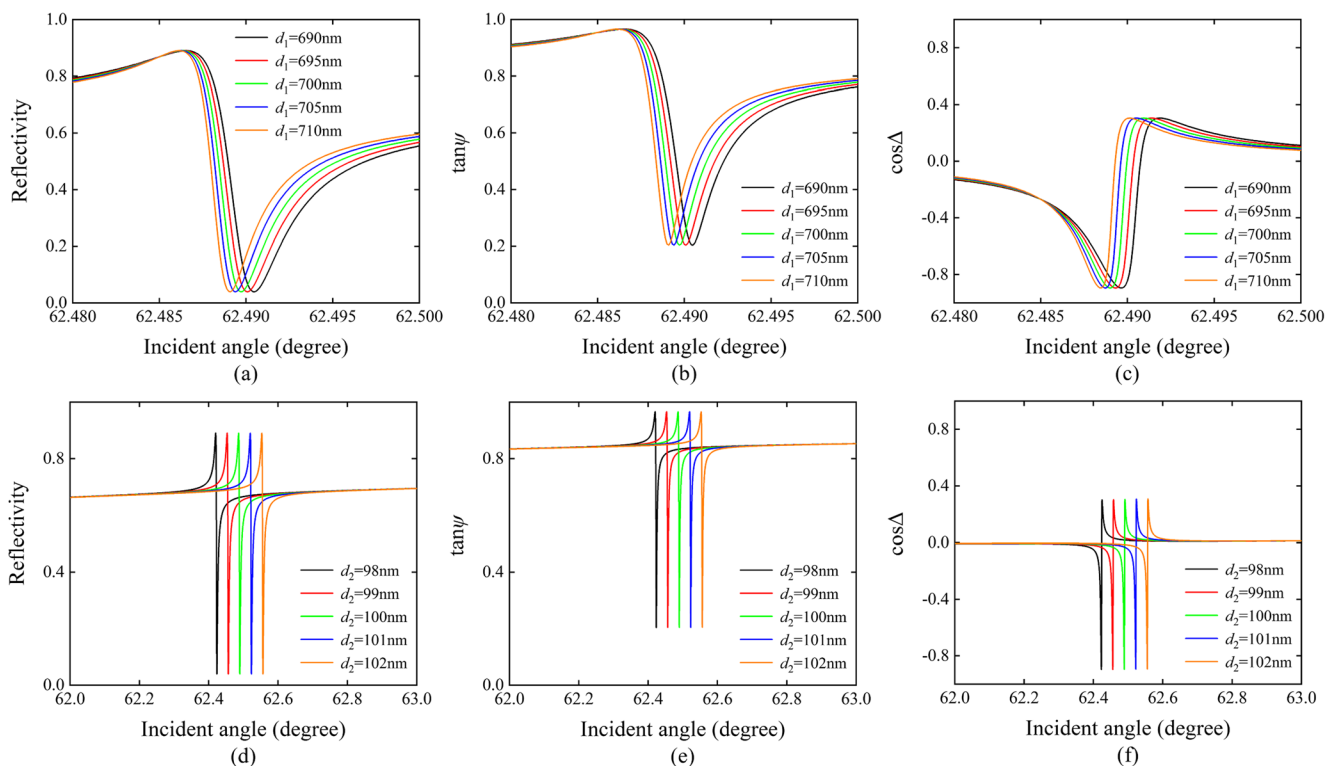$$\text{FOM} = \frac{\text{SL}\cdot S_\theta}{Y_{\max}-Y_{\min}} \quad (15)$$

Fig. 2 The resonance line shape features of both polarization functions and reflectivity obtained for the different cytop (**a–c**) and TiO$_2$ (**d–f**)

where S_θ is the angular sensitivity which is connected with the spectral shifts of the resonance angle as a function of the analyte RI and defined as $S_\theta = \partial\theta_{res} / \partial n_s \cong <\Delta\theta_{res}>_{min} / <\Delta n>_{min}$, where $<\Delta n>_{min}$ is the minimum detectable dielectric change of sensing medium, $<\Delta\theta_{res}>_{min}$ is the corresponding SPR angle change, SL is the slope around the extreme point and is about to $(Y_{max} - Y_{min})$/FWHM, where Y_{max} and Y_{min} are the maximal and minimal values of the corresponding functions from the measurement spectra, and FWHM is the full width at half maximum of that extremum. Under the conditions above, the DL of the system can be expressed by the following:

$$\langle \Delta n \rangle_{min} = \frac{\langle \Delta Y \rangle_{min}}{FOM \cdot (Y_{max} - Y_{min})} \quad (16)$$

where $<\Delta Y>_{min}$ is the noise value of the signal that is directly measured, here Y is $\cos\Delta$ or $\tan\psi$. It can be found from the above equation that the system noise, the SL, and the noise value of the signal are important parameters to decide the level of DL; therefore, by optimizing the structure of the sensor and choosing an appropriate polarization functions can enhance the DL.

Results and Discussion

In order to obtain the optimized parameters for the proposed configuration, the thickness of TiO$_2$ (d_2), which plays an important role in coupling between the SPP and PWG modes, is considered firstly. Since the coupling strength between two modes is related to their effective refractive indices, the effective refractive indices of two modes and their corresponding angle of excitation versus the thickness of d_2 are plotted in Fig. 3. A standard equation for the propagation constant of the SPP together with the above values of the refractive indices yields 1.4516 for the effective refractive index real part of the SPP mode. The propagation constant of a surface plasmon β_{sp} propagating along a planar boundary be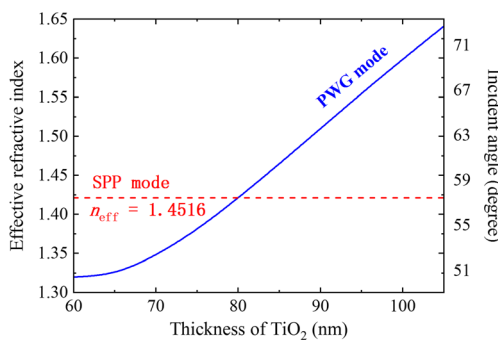tween a semi-infinite metal with a complex permittivity ε_m and a semi-infinite dielectric with a refractive index n can be expressed as follows [45]:

$$\beta_{sp} = \frac{\omega}{c} \sqrt{\frac{n^2 \varepsilon_m}{n^2 + \varepsilon_m}} = \frac{\omega}{c} \left(n_{ef} + i\gamma_i \right) \quad (17)$$

where ω is the angular frequency and c is the speed of light in vacuum. This equation yields a real part of effective index of 1.4516 for the SPP mode. And the effective refractive index of the PWG mode has been calculated by Lumerical FDTD simulation. The effective refractive indices of two modes are equal at this value. The effective refractive index of PWG mode increases with the increasing value of d_2 and approaches the one of SPP mode at a thickness of 80 nm. When the two structures get close, the evanescent fields of SPP mode and PWG mode interact with each other, resulting in mode hybridization. Figure 4 plots the electric field distributions of the proposed structure, where the thickness of cytop and TiO$_2$ are 800 nm and 80 nm, respectively. The effective refractive indices of two modes are equal at this value.

Figure 5 a exhibits the spectral curve of the reflectivity as a function of the incident angle with d_2 ranging from 60 to 120 nm. To obtain the curves, the thickness of cytop (d_1) is fixed at 800 nm. It can be seen that there is large difference in the effective refractive index between two modes even with a d_2 thickness of 60 nm. Thus, two resonance peaks appeared on all of the spectrograms. The effective refractive index of PWG mode is close to that of SPP mode with increasing of d_2 firstly. The resonance peak of SPP mode remains in the same position, while that of PWG mode is gradually moving to larger angle at the same time. Under this condition, an asymmetrical sharp resonance, namely FR, appears in
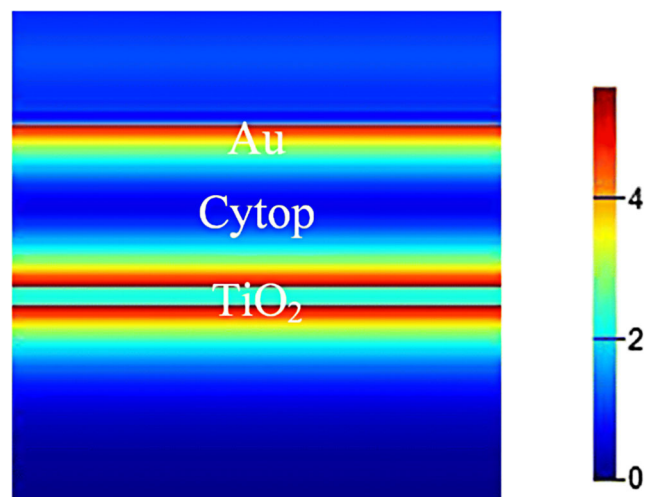

Fig. 3 Effective indices of SPP mode and PWG mode with respected to different TiO$_2$ thickness

Fig. 4 The field distributions of the proposed configuration with when the effective refractive indices of two modes are equal
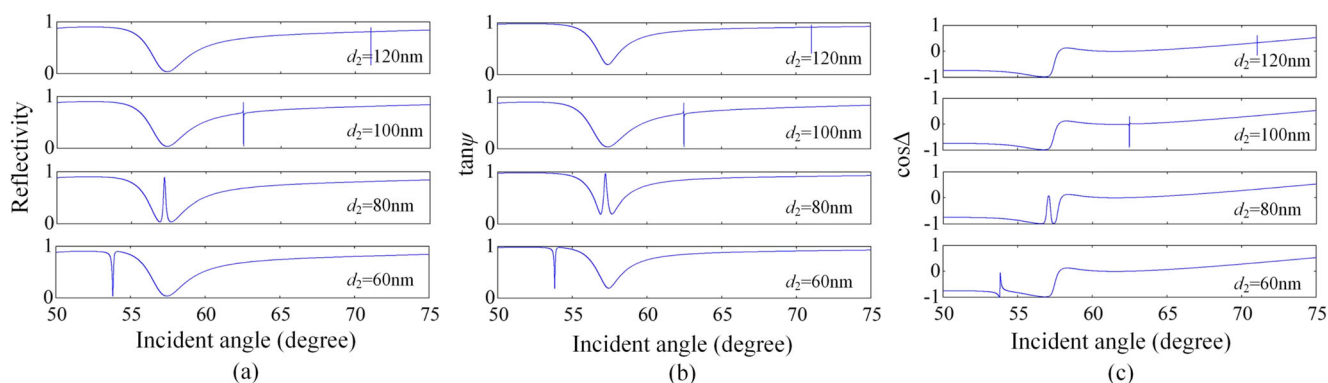
Fig. 5 **a** Reflectivity, **b** $\tan\psi$, and **c** $\cos\Delta$ as functions of d_2 ranging from 60 to 120 nm

the spectrum caused by mode coupling. With further increment of the d_2, the FR peak continues right-shifting from SPP resonance dip and the resonance depth becomes less shallow. Similar phenomenon can be found for polarization functions $\tan\psi$ Fig. 5b and $\cos\Delta$ Fig. 5c.

To further investigate the spectrum of FR and the performance of the sensor, the SL and sensitivity of the extreme point for both polarization functions and reflectivity are plotted as a function of d_2 as shown in Fig. 6. When the steep part of the FR spectrum is used for sensing, the slope of that part determines the performance [10]. An optimal response for functions means that we get the steepest slope at the extreme point. Figure 6 a–c indicate that the SL of all functions' extreme points shifted towards to a peak value firstly and then decreased when the value of d_2 increased. For larger d_2, the coupling strength of both modes decreases, resulting in the drastic decay of resonance. Combination with Fig. 5 and Fig. 6, there is an interesting phenomenon that the value of

SL is not optimal when the effective refractive index of the two modes is equal. In other words, the best coupling efficiency of the two modes is not conducive to improving the performance of the sensor. The extreme points of each function have different optimal values. The minimum of $\cos\Delta$ offers the largest slope for its amplitude is twice that of the reflectivity and $\tan\psi$, then comes minimum of $\cos\Delta$ for the same reason, after that is the minimum of the reflectivity, then comes the minimum of $\tan\psi$, and finally comes the maximum of reflectivity and $\tan\psi$ with the same degrees. Figure 6 d exhibits the sensitivity of different functions' extrema. It is seen that with the increase of d_2, all functions' extrema have nearly the same sensitivity. Compared with the conventional SPR sensor, the sensor based on FR cannot provide better angular sensitivity, but the SL near the extrema is sharp enough to obtain a better DL. By evaluating the sensing performance according to the conditions above, it seems that the minimum of both polarization functions and reflectivity have

Fig. 6 The SL of the extrema of (a) reflectivity, (b) $\tan\psi$ and (c) $\cos\Delta$, and (d) the angular sensitivity of all functions on the thickness of d_2. The sensitivity of different extreme point of a function is the same
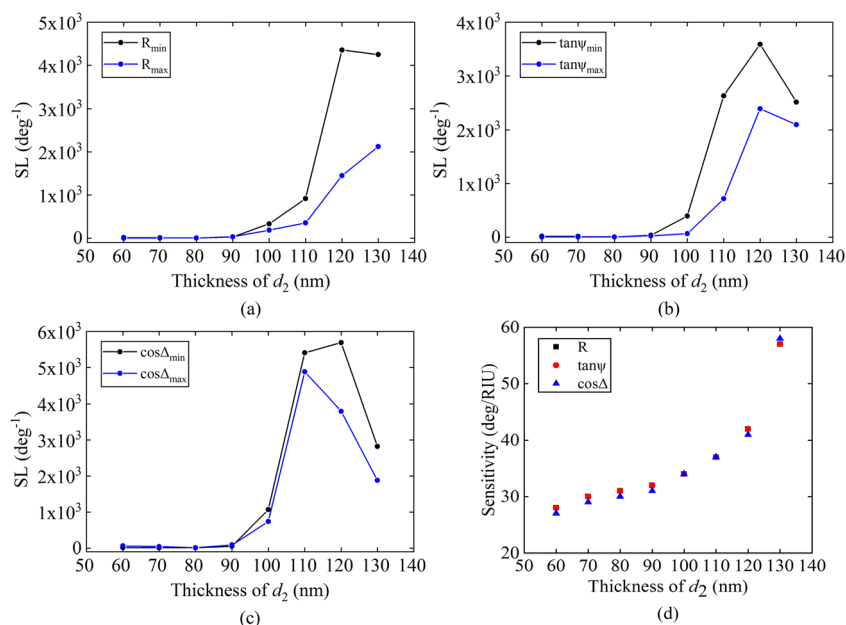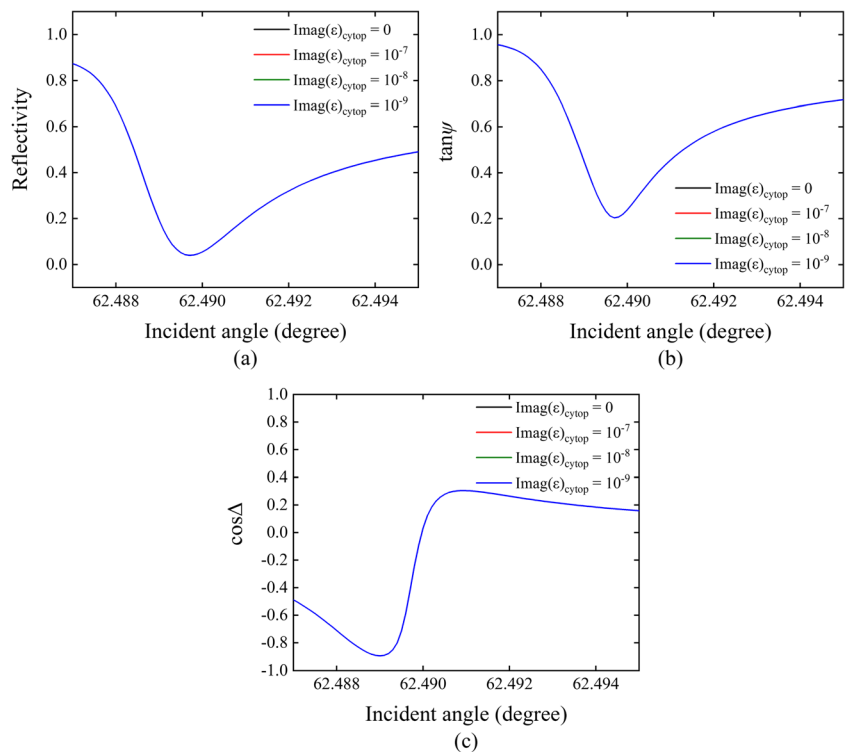
Fig. 7 Dependence of resonance line shape features of **a** reflectivity, **b** $\tan\psi$ and **c** $\cos\Delta$ on the imaginary part of dielectric constant of cytop

preferable performance. In our calculation, the absorption loss of TiO$_2$ has been taken into consideration with $\mathrm{Imag}(\varepsilon)_{\mathrm{TiO2}} = 8.0680 \times 10{-}9$ [46]. The resonance features of both polarization functions and reflectivity obtained for different imaginary part of dielectric constant of cytop, $\mathrm{Imag}(\varepsilon)_{\mathrm{cytop}}$, are represented in Fig. 7. It can be found that there is no obvious variation within 0, $10^{-7}, 10^{-8}$, and 10^{-9}.

In addition to the above conditions, the noise level of the SPR signal is also an important parameter that affects the DL. To illustrate the effects of TiO$_2$ thickness on the polarization functions and reflectivity, the variations of the noise respect to the different d_2 are drawn in Fig. 8. The intensity of the incident light is 24,000 counts, the rotating stage precision of analyzer is 0.5 mdegs, and the mean intensity noise is 10 counts [42]. There is an interesting phenomenon that the noise of the polarization functions has a strong enhancement at the position of the resonance, and the noise decreases with d_2 increment. It means that the resonance peaks of $\tan\psi$ are more easily affected by the noise if they are closer to 0. For the polarization function $\cos\Delta$, the minima can also be disturbed by the noise more drastically than the maxima. On the contrary, the noise of the reflectivity reaches the minimum at the resonance peak and reaches the highest at maximum. It contradicts the claim that the minima of polarization functions have preferable performance. In order to obtain the optimal function and thickness of d_2 for better DL, the effects of two factors above need to be considered, simultaneously.

Figure 9 shows the DL with different thickness of TiO$_2$ based on polarization functions and reflectivity. It can be found when $R_{\min}$, $\tan\psi_{\min}$, $\tan\psi_{\max}$, and $\cos\Delta_{\min}$ are used to represent the sensing performance, the optimal value of d_2 is 120 nm, while that of $R_{\max}$ and $\cos\Delta_{\max}$ are 130 nm and 110 nm, respectively. Furthermore, the advantage in detecting FR is that we can detect two extrema simultaneously at each measurement. In this way, the accuracy of detection can be significantly improved in comparison to the conventional reflectivity measurement based on SPR where there is only one extremum detected [31]. From the results above, it is shown that when the system noise is taken into consideration, $\cos\Delta_{\min}$ is no longer the best choice, $\cos\Delta_{\max}$ offers an optimal DL, whereas $R_{\max}$ provides the worst performance. The influence of noise plays a dominant role when measuring the DL. Also, it can be seen that the optimal thickness of TiO$_2$ is varied with different functions' extrema; therefore, the interrogation method can be chosen according to the achievable thickness of TiO$_2$ during fabrication.

Besides the waveguide layer, the thickness of spacer layer, where the evanescent fields of two modes interact with each other, also affects the DL of the sensor. The variation of the DL versus the thickness of spacer layer (d_1) of different functions are shown in Fig. 10; d_2 of different functions are chosen as the optimal value corresponding to each one. It is clear that there is an optimal thickness for sensing performance and the performance decreases as the thickness continues to increase. The evanescent fields' overlap of the SPP and PWG modes occurs

Fig. 8 Spectra of the noise **a**, **b** <ΔR>, **c**, **d** <Δtanψ>, and **e**, **f** <ΔcosΔ> in the polarimetric functions reflectivity, tanψ, and cosΔ, respectively, for different thicknesses of the d_2, using the noise values $\Delta A = 0.5$ mdegs, and $\Delta I = 10$ counts, assuming a spectrally constant light source intensity of $I_0 = 24{,}000$ counts
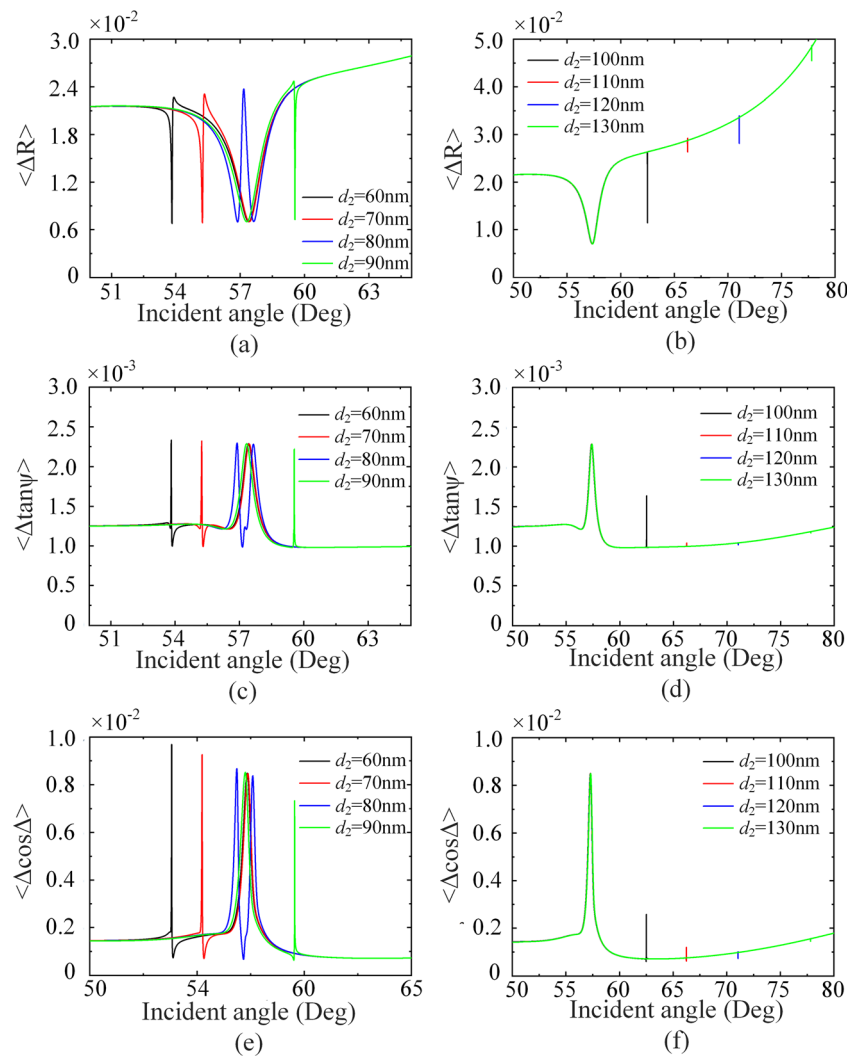

Fig. 9 DL versus the thickness of d_2 based on the different functions' extrema. **a** R, **b** tanψ, and **c** cosΔ
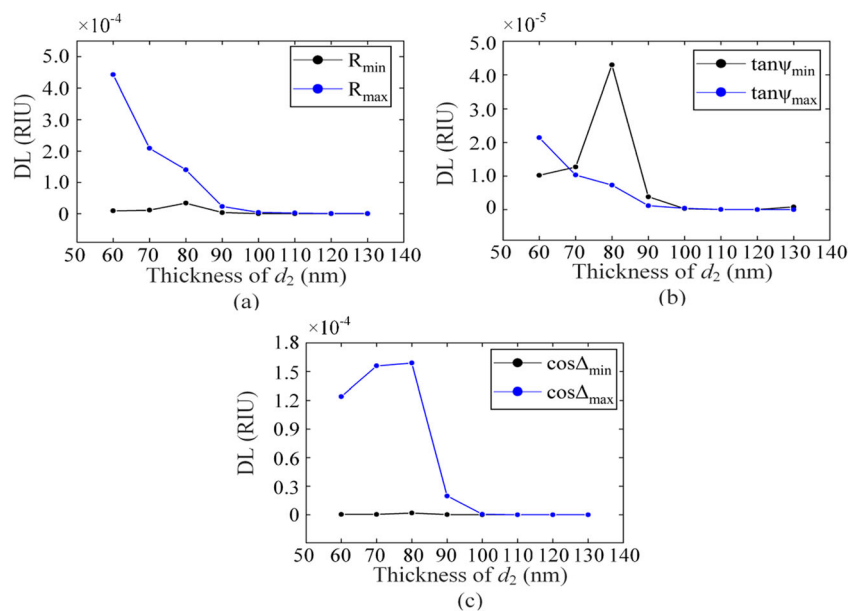
Fig. 10 DL versus the thickness of d_1 based on the different functions' extrema. **a** R, **b** tanψ, and **c** cosΔ
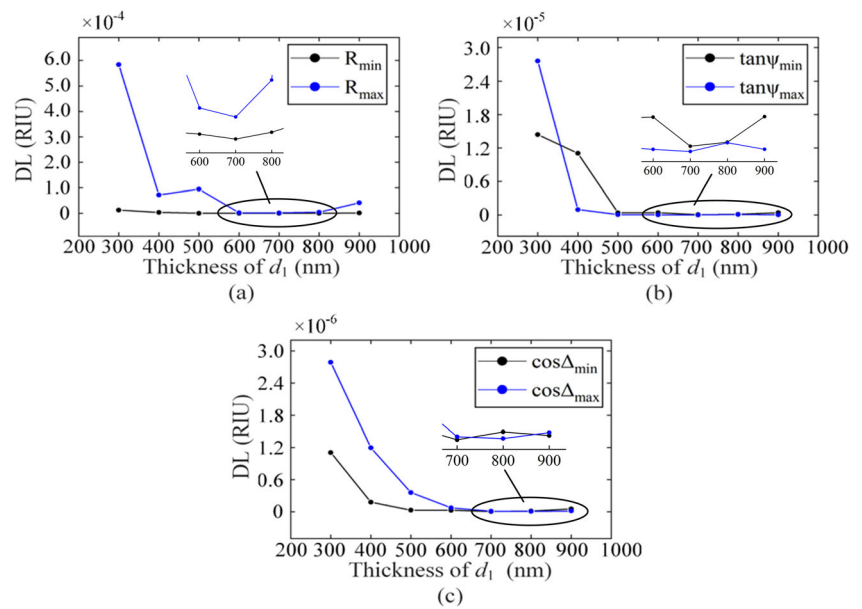

Table 1 Optimized parameters of proposed structure with different types of extrema corresponding DL

Type of extreme point	R_{min}	R_{max}	tanψ_{min}	tanψ_{max}	CosΔ_{min}	CosΔ_{max}
Optimum thickness of d_1 (nm)	700	700	700	700	700	800
Optimum thickness of d_2 (nm)	120	130	110	120	120	110
DL (RIU)	6.21×10^{-8}	1.75×10^{-6}	3.71×10^{-8}	7.20×10^{-9}	6.20×10^{-9}	8.50×10^{-9}

in the spacer layer d_1, which determines the coupling strength. A thicker coupling layer results in a weaker coupling. According to our calculation, the optimum thickness of cytop for R_{min}, R_{max}, tanψ_{min}, tanψ_{max}, and cosΔ_{min} is 700 nm, while that for cosΔ_{max} is 800 nm. The corresponding DLs based on different polarization functions and reflectivity are summarized in Table 1. The optimized DL of R_{min}, R_{max}, tanψ_{min}, tanψ_{max} cosΔ_{min}, and cosΔ_{max} are 6.21×10^{-8}, 1.75×10^{-6}, 3.71×10^{-8}, 7.20×10^{-9}, 6.20×10^{-9}, and 8.50×10^{-9}, respectively.

In the field of biosensing, how to detect DNA hybridization is a crucial step. The complicated functionalization process has been a challenging area. Tikhomirov et al. employed a one-pot process that could synthesize bright, stable CdTe nanocrystal quantum dots functionalized with DNA. Mercaptopropionic acid (MPA) was used as a co-ligand to passivate sites left open by the DNA. The DNA ligands here consisted of three domains: a quantum-dot-binding domain featuring phosphorothioate linkages within the backbone; a spacer containing phosphodiester linkages; and it is worth noting that a DNA-binding domain also composed of a sequence with phosphodiester linkages. This unbound part of the DNA ligand can be used for specific binding to complementary segments from different points [47]. Li et al. propose a biosensor based on optical bistability in a biological semiconductor quantum dot (SQD)-DNA coupled nanohybrid.

With its size-dependent, bright, and stable fluorescence properties, SQD is often used as a tool for studying many biological and biomedical problems such as bioimaging, photothermal therapy, and targeted drug delivery. When
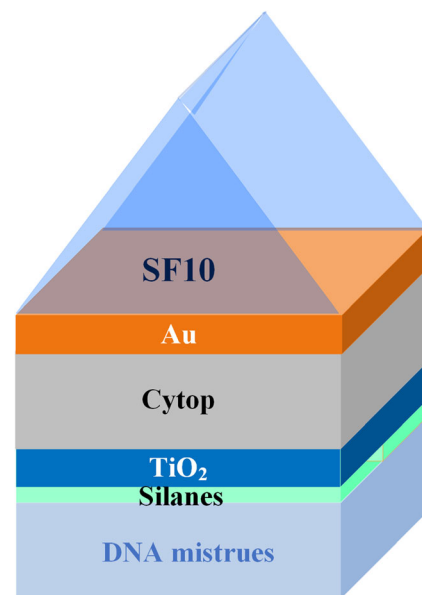

Fig. 11 The structure diagram of improved sensor structure used to detect DNA hybridization

Fig. 12 The variation of resonance spectra of **a** reflectivity, **b** tanψ and **c** cosΔ with DNA renaturation. The red arrow indicates the DNA renaturation, in which the change of percentage renaturation of ssDNA is 10% each time. **d** The angular sensitivity of all functions versus the percentage renaturation. The sensitivity of different extreme point of a function is the same
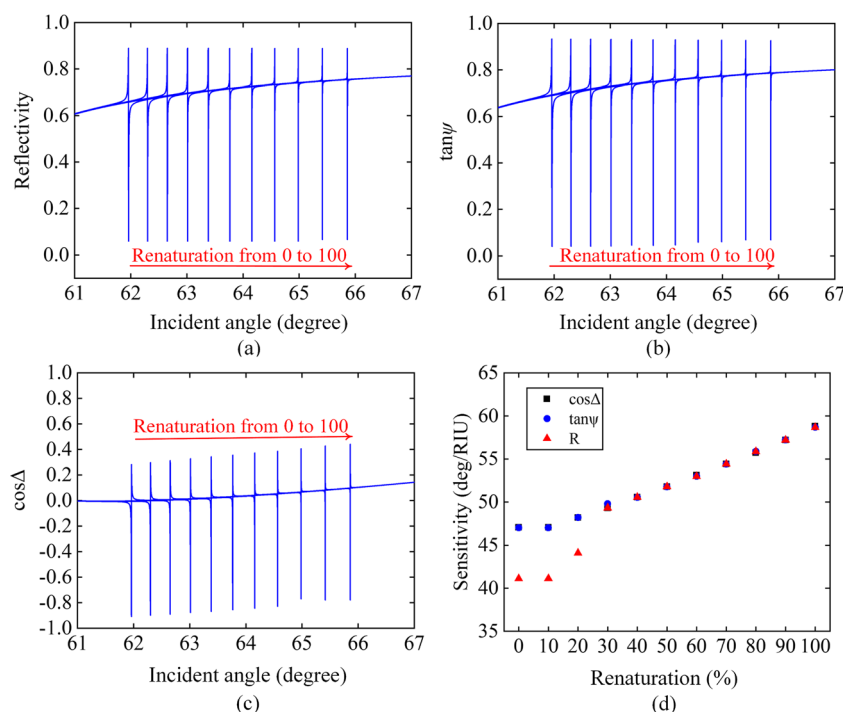
SQD is strongly coupled with DNA molecule, the vibrational mode of DNA molecule has a great influence on SQD energy level. In addition, optical bistability is highly sensitive to DNA molecular length, DNA concentration, and DNA-DNA coupling strength [48]. Renaturation is a process in which single-stranded DNA (ssDNA) can reformulate hydrogen bonds between complementary strands of ssDNA, which allowed it to reform double-stranded DNA (dsDNA) structure [49]. Here, the DNA hybridization process can be overcome by using label-free detection involving linker layer to replace conventional targeted DNA sequence [50]. The improved sensor structure used to detect DNA hybridization is shown in Fig. 11, in which the metal thickness is fixed at 50 nm, and the thickness of cytop and TiO$_2$ are 700 nm and 80 nm respectively, which makes the SPP mode and the PWG mode strongly coupled to facilitate detection of DNA hybridization. Silanes of 1 nm is sandwiched between TiO$_2$ and DNA as a connecting layer with a refractive index of 1.42 [51]. The connecting layer and DNA are arranged in an aqueous solution. Conversion between dsDNA and ssDNA is described by the refractive index of the dsDNA-ssDNA mixture at different percentages obtained by the Lorentz-Lorenz mixing rule given as follows [52]:

$$\frac{n^2_{ab}-1}{n^2_{ab}+2} = \phi_a \left(\frac{n^2_a-1}{n^2_a+2} \right) + \phi_b \left(\frac{n^2_b-1}{n^2_b+2} \right) \quad (18)$$

where n_a and n_b are the refractive index of ssDNA and dsDNA respectively, which are 1.456 and 1.53, and n_{ab} is employed to represent the refractive index of ssDNA-dsDNA mixture. φ_a and φ_b are volume fractions of ssDNA and dsDNA. After

rearrangement, the refractive index of the dsDNA-ssDNA mixture can be given as:

$$n_{ab} = \sqrt{\frac{(n^2_a+2)(n^2_b+2)+2[\phi_a(n^2_a-1)(n^2_b+2)+\phi_b(n^2_a+2)(n^2_b-1)]}{(n^2_a+2)(n^2_b+2)-[\phi_a(n^2_a-1)(n^2_b+2)+\phi_b(n^2_a+2)(n^2_b-1)]}}$$

$$(19)$$

In the renaturation process, the resonance spectrum and sensitivity of polarization function are detected firstly. Resonance changes of renaturation of different functions are drawn in Fig. 12a–c. Formation of dsDNA will alter the refractive index of the ssDNA-dsDNA mixture. By observing the resonance spectrum as a function of refractive index, the ratio of ssDNA and dsDNA in mixtures can be detected to
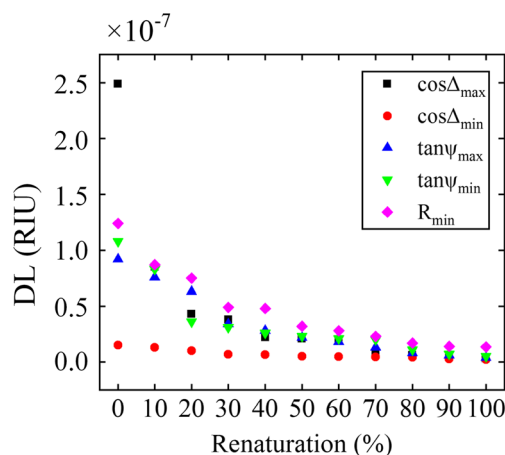

Fig. 13 DL of different extreme points of a function versus the percentage renaturation of ssDNA

Table 2 DL of various label-free DNA sensors

Technology platform	Structure	Detection limits (RIU)
Surface plasmon resonance	Prism coupler–based SPR sensor	5×10^{-7} [53]
	Grating coupler–based SPR sensor	2×10^{-6} [53]
	White-light spectral interferometry–based SPR sensor	2×10^{-8} [54]
Optical microfiber	Microfiber-assisted Mach-Zehnder interferometer	4.32×10^{-5} [55]
Optical fiber	Fiber-optic–based biosensing	2×10^{-4} [56]
Ring resonator	Slot waveguide–based ring resonator biosensor	1.43×10^{-6} [57]
	Opto-fluidic ring resonators	1×10^{-7} [58]
This work	Three-point method–based Fano sensor	2.1×10^{-9}

estimate the hybridization process of DNA. Sensitivity of the proposed Fano resonance sensors with different functions is plotted in Fig. 12d; careful comparison leads to the conclusion that there is not much difference in the sensitivity of different functions.

Considering the influence of noise on the sensing performance, Fig. 13 shows the DLs of different functions during the DNA renaturation. Obviously, with the progress of DNA renaturation, ssDNA is converted to dsDNA and the DL of the sensor decreases gradually. Meanwhile, the polarization functions have better DL than reflectivity. When DNA renaturation reaches 100, ssDNA is completely converted to dsDNA; the sensor has a lowest DL with the function of $\cos\Delta_{min}$, which can reach 2.1×10^{-9}. The function of $\cos\Delta_{max}$, $\tan\psi_{max}$ and $\tan\psi_{min}$ has similar DLs, about 4.0×10^{-9}. At the end is R_{min} whose DL is 1.5×10^{-8}, which is an order of magnitude larger than the polarization functions. The result of simulation is the same as the conclusion in this paper.

For comparison, the performances of previously reported optical label-free DNA sensors are summarized in Table 2. There is an obvious enhancement on detection limits in the proposed polarimetric sensor.

Conclusions

In this paper, a hybrid structure consisting of SF10 glass, Au layer, cytop spacer layer, TiO_2 waveguide layer, and sensing medium is proposed to generate strong and sharp Fano resonant signals. Specifically, the angular three-point measurement method is employed and demonstrated for the first time to explore the FR-based sensing performance. Two polarization functions ($\tan\psi$ and $\cos\Delta$) and reflectivity (R) are analyzed and compared to evaluate the system performance. It is shown that when the system noise is taken into consideration in the configuration, the optimized sensor is different from the noise-free one. According to the analysis, the lowest DL up to 6.20×10^{-9} RIU can be obtained by using polarization function $\cos\Delta_{min}$ as the interrogation object. Renaturation of DNA is simulated to confirm the research we propose. The results are consistent with our study that the polarization functions have a lower DL. Thus, we believe that the proposed FR-based sensor can be a promising and useful platform in the areas of biochemical sensing.

References

1. Huang YH, Ho HP, Kong SK, Kabashin AV (2012) Phase-sensitive surface plasmon resonance biosensors: methodology, instrumentation and applications. Ann Phys 524:637–662
2. Kretschmann E, Raether H (1968) Notizen: Radiative decay of nonradiative surface plasmons excited by light. Zeitschrift für Naturforschung A 23:2135–2136
3. Ahn H, Song H, Choi JR, Kim K (2017) Localized surface plasmon resonance sensor using double-metal-complex nanostructures and a review of recent approaches. Sensors 18:98
4. Zeng S, Baillargeat D, Ho HP, Yong KT (2014) Nanomaterials enhanced surface plasmon resonance for biological and chemical sensing applications. Chem Soc Rev 43:3426–3452
5. Zeng S, Sreekanth KV, Shang J, Yu T, Chen CK, Yin F, Baillargeat D, Coquet P, Ho HP, Kabashin AV, Yong KT (2015) Graphene–gold metasurface architectures for ultrasensitive plasmonic biosensing. Adv Mater 27:6163–6169
6. Tan XJ, Zhu XS (2016) Enhancing photonic spin Hall effect via long-range surface plasmon resonance. Opt Lett 41:2478–2481
7. Ahn JH, Seong TY, Kim WM, Lee TS, Kim I, Lee KS (2012) Fiber-optic waveguide coupled surface plasmon resonance sensor. Opt Express 20:21729–21738
8. Zhu J, Li JJ, Yuan L, Zhao JW (2012) Optimization of three-layered Au–Ag bimetallic nanoshells for triple-bands surface plasmon resonance. J Phys Chem C 116:11734–11740
9. Hayashi S, Nesterenko DV, Sekkat Z (2015) Fano resonance and plasmon-induced transparency in waveguide-coupled surface plasmon resonance sensors. Appl Phys Express 8:022201
10. Hayashi S, Nesterenko DV, Sekkat Z (2015) Waveguide-coupled surface plasmon resonance sensor structures: Fano lineshape engineering for ultrahigh-resolution sensing. J Phys D Appl Phys 48:325303–325313

11. Nesterenko DV, Hayashi S, Sekkat Z (2016) Extremely narrow resonances, giant sensitivity and field enhancement in low-loss waveguide sensors. J Opt 108:065004

12. Wu L, Guo J, Xu H, Dai X, Xiang Y (2016) Ultrasensitive biosensors based on long-range surface plasmon polariton and dielectric waveguide modes. Photonics Research 4:262–266

13. Li L, Huang T, Zhao X, Wu X, Cheng Z (2018) Highly sensitive SPR sensor based on hybrid coupling between plasmon and photonic mode. IEEE Photon Technol Lett 30:1364–1367

14. Huang T, Zeng S, Zhao X, Cheng Z, Shum PP (2018) Fano resonance enhanced surface plasmon resonance sensors operating in near-infrared. Photonics 5:23

15. Kabashin AV, Patskovsky S, Grigorenko AN (2009) Phase and amplitude sensitivities in surface plasmon resonance bio and chemical sensing. Opt Express 17:21191–21204

16. Zheng Z, Wan Y, Zhao X, Zhu J (2009) Spectral interferometric measurement of wavelength-dependent phase response for surface plasmon resonance sensors. Appl Opt 48:2491–2495

17. Zhang Y, Li H, Duan J, Shi A, Liu Y (2013) Surface plasmon resonance sensor based on spectral interferometry: numerical analysis. Appl Opt 52:3253–3259

18. Su YD, Chen SJ, Yen TL (2005) Common path phase shift interferometry surface plasmon resonance imaging system. Opt Lett 30:1488

19. Yuan W, Ho HP, Wong CL, Kong SK, Lin C (2007) Surface plasmon resonance biosensor incorporated in a Michelson interferometer with enhanced sensitivity. IEEE Sensors J 7:70–73

20. Yuan W, Ho HP, Suen YK, Kong SK, Lin C (2007) Improving the sensitivity limit of surface plasmon resonance biosensors by detecting mixed interference signals. Appl Opt 46:8068–8073

21. Ng SP, Wu CML, Wu SY, Ho HP (2011) White-light spectral interferometry for surface plasmon resonance sensing applications. Opt Express 19:4521–4527

22. Hlubina P, Duliakova M, Kadulova M, Ciprian D (2015) Spectral interferometry-based surface plasmon resonance sensor. Opt Commun 354:240–245

23. Xinglong Y, Lequn Z, Hong J, Haojuan W, Chunyong Y, Shenggeng Z (2001) Immunosensor based on optical heterodyne phase detection. Sensors Actuators B Chem 76:199–202

24. Wu CM, Jian ZC, Joe SF, Chang LB (2003) High-sensitivity sensor based on surface plasmon resonance and heterodyne interferometry. Sensors Actuators B Chem 92:133–136

25. Kuo WC, Chou C, Wu HT (2003) Optical heterodyne surface-plasmon resonance biosensor. Opt Lett 28:1329–1331

26. Chiu MH, Wang SF, Chang RS (2005) D-type fiber biosensor based on surface-plasmon resonance technology and heterodyne interferometry. Opt Lett 30:233–235

27. Chou C, Wu HT, Huang YC, Chen YL, Kuo WC (2006) Characteristics of a paired surface plasma waves biosensor. Opt Express 14:4307–4315

28. Naraoka R, Kajikawa K (2005) Phase detection of surface plasmon resonance using rotating analyzer method. Sensors Actuators B Chem 107:952–956

29. Markowicz PP, Law WC, Baev A, Prasad P, Patskovsky S, Kabashin AV (2007) Phase-sensitive time modulated SPR polarimetry for wide dynamic range biosensing. Opt Express 15:1745–1754

30. Patskovsky S, Jacquemart R, Meunier M, De Crescenzo G, Kabashin AV (2008) Phase-sensitive spatially modulated surface plasmon resonance polarimetry for detection of biomolecular interactions. Sensors Actuators B Chem 133:628–631

31. Phan QH, Yang PM, Lo YL (2015) Surface plasmon resonance prism coupler for gas sensing based on Stokes polarimetry. Sensors Actuators B Chem 216:247–254

32. Watad I, Abdulhalim I (2017) Spectropolarimetric surface plasmon resonance sensor and the selection of the best polarimetric function. IEEE J Sel Top Quant Electron 23:89–97

33. Markowicz PP, Law WC, Baev A, Prasad PN, Patskovsky S, Kabashin AV (2007) Phase-sensitive time-modulated surface plasmon resonance polarimetry for wide dynamic range biosensing. Opt Express 15:1745–1754

34. Zeng S, Hu S, Xia J, Anderson T, Dinh XQ, Meng XM, Coquet P, Yong KT (2015) Graphene–MoS2 hybrid nanostructures enhanced surface plasmon resonance biosensors. Sensors Actuators B Chem 207:801–810

35. Kawasaki M, Chen M, Yang J, Chiou W, Shiojiri M (2013) Structural analysis of Au/TiO2 thin films deposited on the glass substrate. Appl Phys Lett 102:091603

36. Daviau R, Khan A, Lisicka-Skrzek E, Tait R, Berini P (2010) Fabrication of surface plasmon waveguides and integrated components on Cytop. Microelectron Eng 87:1914–1921

37. Besserguenev VG, Pereira R, Mateus MC, Khmelinskii IV, Nicula RC, Burke E (2003) TiO2 thin film synthesis from complex precursors by CVD, its physical and photocatalytic properties. Int J Photoenergy 5:99–105

38. Lukosz W, Stamm C (1990) Integrated optical interferometer as relative humidity sensor and differential refractometer. Sensors Actuators A Phys 25:185–188

39. Boecker D, Zybin A, Niemax K, Grunwald C, Mirsky VM (2008) Noise reduction by multiple referencing in surface plasmon resonance imaging. Rev Sci Instrum 79:3110–0231

40. Watad I, Jabalee MA, Aizen A, Abdulhalim I (2015) Critical-angle-based sensor with improved figure of merit using dip detection. Opt Lett 40:4388–4391

41. Wang X, Jefferson M, Hobbs PC, Risk WP, Feller BE, Miller RD, Knoesen A (2011) Shot-noise limited detection for surface plasmon sensing. Opt Express 19:107–117

42. Ibrahim W, Ibrahim A (2017) Comparative study between polarimetric and intensity-based surface plasmon resonance sensors in the spectral mode. Appl Opt 56:7549–7558

43. Nenninger GG, Piliarik M, Homola J (2002) Data analysis for optical sensors based on spectroscopy of surface plasmons. Meas Sci Technol 13:2038–2046

44. Marks RS, Abdulhalim I (2016) Nanomaterials for water management: signal amplification for biosensing from nanostructures. Anal Bioanal Chem 408:3673–3674

45. Piliarik M, Homola J (2009) Surface plasmon resonance (SPR) sensors: approaching their limits? Opt Express 17:16505–16517

46. Siefke T, Kroker S, Pfeiffer K, Puffky O, Dietrich K, Franta D, Ohlídal I, Szeghalmi A, Kley E-B, Tünnermann A (2016) Materials pushing the application limits of wire grid polarizers further into the deep ultraviolet spectral range. Adv Opt Mater 4:1780–1786

47. Tikhomirov G, Hoogland S, Lee PE, Fischer A, Sargent EH, Kelley SO (2011) DNA-based programming of quantum dot valency, self-assembly and luminescence. Nat Nanotechnol 6:485–490

48. Li J, Liang S, Xiao S, He M, Liu L, Luo J, Chen L (2019) A sensitive biosensor based on optical bistability in a semiconductor quantum dot-DNA nanohybrid. J Phys D Appl Phys 52:035401

49. Singh RR, Priye V (2018) Silicon nanowire optical rectangular waveguide (SNORW) biosensor for DNA hybridization. IEEE Photon Technol Lett 30:1123–1126

50. Barozzi M, Manicardi A, Vannucci A, Candiani A, Sozzi M, Konstantaki M, Pissadakis S, Corradini R, Selleri S, Cucinotta A (2017) Optical Fiber sensors for label-free DNA detection. J Lightwave Technol 35:3461–3472

51. Dar T, Homola J, Rahman B, Rajarajan M (2012) Label-free slotwaveguide biosensor for the detection of DNA hybridization. Appl Opt 34:8195–8202

52. Aleksandar ZT, Djordjevic BD, Grozdanic DK, Radojkovic N (1992) Use of mixing rules in predicting refractive indexes and specific refractivities for some binary liquid mixtures. J Chem Eng Data 37:310–313

53. Homola J, Yee SS, Gauglitz G (1999) Surface plasmon resonance sensors: review. Sensors Actuators B Chem 54:3–15

54. Loo FC, Ng SP, Wu CL, Kong SK (2014) An aptasensor using DNA aptamer and white light common-pathSPR spectral interferometry to detect cytochrome-c for anti-cancerdrug screening. Sensors Actuators B Chem 198:416–423

55. Song B, Zhang H, Liu B, Lin W, Wu J (2016) Label-free in-situ real-time DNA hybridization kinetics detection employing microfiber-assisted Mach-Zehnder interferometer. Biosens Bioelectron 81:151–158

56. Pollet J, Delporta F, Janssen KPF, Jans K, Maes G, Pfeiffer H, Wevers M, Lammertyn J (2009) Fiber optic SPR biosensing of DNA hybridization and DNA–protein interactions. Biosens Bioelectron 25:864–869

57. Dar T, Homola J, Azizur Rahman BM, Rajarajan M (2012) Label-free slot-waveguide biosensor for the detection of DNA hybridization. Appl Opt 51:8195–8202

58. Suter JD, Howard DJ, Shi H, Caldwell CW, Fan X (2010) Label-free DNA methylation analysis using opto-fluidic ring resonators. Biosens Bioelectron 26:1016–1020